Article

The causes of sea-level rise since 1900

Thomas Frederikse[1 ✉], Felix Landerer[1], Lambert Caron[1], Surendra Adhikari[1], David Parkes[2], Vincent W. Humphrey[3], Sönke Dangendorf[4,5], Peter Hogarth[6], Laure Zanna[7], Lijing Cheng[8,9] & Yun-Hao Wu[10]

The rate of global-mean sea-level rise since 1900 has varied over time, but the contributing factors are still poorly understood[1]. Previous assessments found that the summed contributions of ice-mass loss, terrestrial water storage and thermal expansion of the ocean could not be reconciled with observed changes in global-mean sea level, implying that changes in sea level or some contributions to those changes were poorly constrained[2,3]. Recent improvements to observational data, our understanding of the main contributing processes to sea-level change and methods for estimating the individual contributions, mean another attempt at reconciliation is warranted. Here we present a probabilistic framework to reconstruct sea level since 1900 using independent observations and their inherent uncertainties. The sum of the contributions to sea-level change from thermal expansion of the ocean, ice-mass loss and changes in terrestrial water storage is consistent with the trends and multidecadal variability in observed sea level on both global and basin scales, which we reconstruct from tide-gauge records. Ice-mass loss—predominantly from glaciers—has caused twice as much sea-level rise since 1900 as has thermal expansion. Mass loss from glaciers and the Greenland Ice Sheet explains the high rates of global sea-level rise during the 1940s, while a sharp increase in water impoundment by artificial reservoirs is the main cause of the lower-than-average rates during the 1970s. The acceleration in sea-level rise since the 1970s is caused by the combination of thermal expansion of the ocean and increased ice-mass loss from Greenland. Our results reconcile the magnitude of observed global-mean sea-level rise since 1900 with estimates based on the underlying processes, implying that no additional processes are required to explain the observed changes in sea level since 1900.

Global-mean sea level (GMSL) has increased by approximately 1.5 mm yr^{-1} (refs. [1,4,5]) over the twentieth century, modulated by large multidecadal fluctuations[6]. Changes in GMSL are the net result of many individual geophysical and climatological processes, with some of the largest contributions coming from ice-mass loss and thermal expansion of the ocean. The level of agreement between the sum of these individual contributions and the observed changes in GMSL—often described as the 'sea-level budget'—is a key indicator of our understanding of the drivers of sea-level rise[7]. Multiple studies show closure of the sea-level budget within their stated uncertainties since the 1960s and over the era of satellite altimetry since 1993[8–10]. However, rates of GMSL change and their contributions to the budget over the entire twentieth century, and especially the first half of the twentieth century, have not yet been fully explained or attributed. Previous observation-based studies concluded that the GMSL budget for the whole twentieth century could not be closed within the estimated uncertainties[2,3]. Various explanations for this non-closure have been proposed, including an overestimation of

the tide-gauge-derived rates of GMSL change[11] and underestimation of the ice-sheet contribution[12], but there is no agreement yet on the cause of this discrepancy[13].

Over the past few years, revised estimates of the main known driving processes of global sea-level rise that cover the entire twentieth century have become available[14–17], the spread among different estimates of twentieth-century glacier mass loss has been reduced[18], and improved mapping methods and correction of instrumental bias have resulted in higher estimates of the contribution from thermal expansion since the 1960s[19]. In parallel, estimates of twentieth-century GMSL change have converged to lower rates than previously estimated, as a result of improved reconstruction approaches, spatial-bias correction schemes, and the inclusion of estimates of local vertical land motion (VLM) at tide-gauge locations[4,9,20]. As a result of these developments, the GMSL budget needs to be re-estimated, to determine whether the observed sea-level rise since 1900 can be reconciled with the estimated sum of contributing processes.

[1]Jet Propulsion Laboratory, California Institute of Technology, Pasadena, CA, USA. [2]Université Catholique de Louvain, Louvain-la-Neuve, Belgium. [3]Division of Geological and Planetary Sciences, California Institute of Technology, Pasadena, CA, USA. [4]Center for Coastal Physical Oceanography, Old Dominion University, Norfolk, VA, USA. [5]University of Siegen, Siegen, Germany. [6]National Oceanography Centre, Liverpool, UK. [7]Courant Institute, New York University, New York, NY, USA. [8]International Center for Climate and Environment Sciences, Institute of Atmospheric Physics, Chinese Academy of Sciences, Beijing, China. [9]Center for Ocean Mega-Science, Chinese Academy of Sciences, Qingdao, China. [10]Research Center for Environmental Changes, Academia Sinica, Taipei, Taiwan. ✉e-mail: thomas.frederikse@jpl.nasa.gov
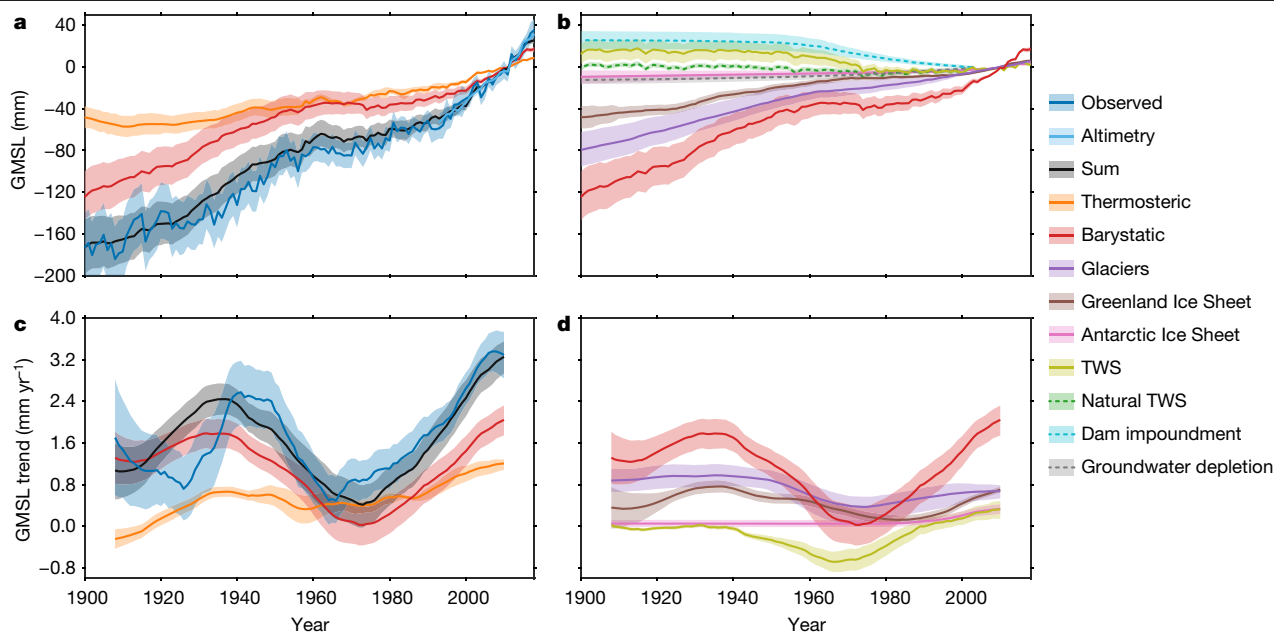
Fig. 1 | Observed GMSL and contributing processes. a, Observed GMSL, and the estimated barystatic and thermosteric contributions and their sum. **b**, The barystatic contribution and its individual components. The TWS term is the sum of groundwater depletion, water impoundment in artificial reservoirs and the natural TWS term. **c**, 30-year-average rates of observed GMSL change and of

GMSL change as a result of the different contributing processes. **d**, 30-year-average rates of GMSL change due to the barystatic contribution and its individual components. The shaded regions denote 90% confidence intervals. The values in **a** and **b** are relative to the 2002–2018 mean.

Estimating the sea-level budget

To obtain estimates of changes in global ocean mass (barystatic changes), we combine estimates of mass change for glaciers[16,21], ice sheets[14,22–25] and terrestrial water storage (TWS). For the TWS estimate, we consider the effects of natural TWS variability[17], water impoundment in artificial reservoirs[26] and groundwater depletion[27,28]. For 2003–2018, we use observations from the Gravity Recovery and Climate Experiment (GRACE)[29] to quantify the barystatic changes. We estimate changes in sea level due to global thermal expansion (thermosteric changes) from in situ subsurface observations[30–32] over the period 1957–2018, and combine these estimates with an existing thermosteric reconstruction[15]. To obtain an estimate of GMSL changes and their accompanying uncertainties, we combine tide-gauge observations with estimates of local VLM from permanent Global Navigation Satellites System (GNSS) stations and with the difference between tide-gauge and satellite-altimetry observations.

Each tide-gauge and VLM record is affected by glacial isostatic adjustment (GIA) and by the effects of gravity, rotation and deformation (GRD) from contemporary surface-mass redistribution due to changes in ice mass and TWS. Owing to the irregular spatial distribution of tide-gauge sites, these effects could bias reconstructed global-mean and basin-mean sea-level changes[33]. To avoid this bias, we remove the local sea-level and VLM imprints from GIA and contemporary GRD effects from each tide-gauge and VLM record before computing basin-mean and global-mean sea-level changes from the tide gauges[9].

We propagate the uncertainties and associated covariances in the sea-level observations, in the contributing processes, and in the GIA and contemporary GRD effects into the final estimates of sea-level changes and the contributing processes. To this end, we generate an ensemble of 5,000 realizations of global-mean and basin-mean sea-level changes and all of the contributing processes. For processes for which multiple estimates are available, such as GIA, we randomly select one of these estimates when computing each individual ensemble member. For processes for which an estimate of the uncertainty is available, such as GNSS observations, we sample the estimate assuming a Gaussian

distribution of the stated uncertainty about the corresponding mean. Then, we compute global-mean and basin-mean sea-level changes and the contributing processes for each ensemble member. We use the ensemble mean and spread to estimate all basin-mean and global-mean sea-level contributions and the associated confidence intervals. See Extended Data Fig. 1 and Methods for a detailed description of our approach.

Global-mean sea level

Our GMSL estimate (Fig. 1a) shows a trend of 1.56 ± 0.33 mm yr^{-1} (90% confidence interval) over 1900–2018. It is also characterized by substantial multidecadal variability, with higher rates of sea-level rise during the 1940s and since the 1990s, and lower rates around 1920 and 1970. The higher rates at the turn of the millennium are in good agreement with independent satellite-altimetry observations[34]. The observed trend over 1900–2018 is consistent with the sum of the estimated thermal expansion and changes in ocean mass, which sum to 1.52 ± 0.33 mm yr^{-1} (90% confidence interval). This consistency holds not only for the trends over the full study period, but also over the past 50 years (Table 1), and for the pattern of multidecadal variability (Fig. 1c), except for the low rates of sea-level change around the 1920s and early 1930s.

Thermosteric and barystatic sea-level changes show similar multidecadal variability patterns to the GMSL changes, although the amplitude of barystatic variability is larger than that of thermosteric variability, and barystatic variability is the main cause of multidecadal GMSL variability (Fig. 1c). The barystatic variability is not dominated by a single process (Fig. 1d). The above-average rate of GMSL rise in the 1940s is largely attributable to above-average contributions from glaciers and the Greenland Ice Sheet, whereas the high rate of barystatic sea-level rise since 2000 is attributable to both the Greenland and Antarctic ice sheets and to TWS. The low rates around 1970 are dominated by the TWS term (Fig. 1d). This negative contribution is caused predominantly by reservoir impoundment. Between 1900 and 2003, $9,400 \pm 3,100$ km^3 (90% confidence interval) of water has been

Table 1 | Linear trends in observed GMSL and in individual contributions to GMSL

	1900–2018 (mm yr⁻¹)	1957–2018 (mm yr⁻¹)	1993–2018 (mm yr⁻¹)
Glaciers	0.70 [0.52, 0.89]	0.52 [0.36, 0.73]	0.67 [0.53 0.84]
Greenland Ice Sheet	0.44 [0.35, 0.53]	0.30 [0.21, 0.38]	0.65 [0.57 0.74]
Antarctic Ice Sheet	0.08 [0.00, 0.17]	0.13 [0.04, 0.22]	0.32 [0.21 0.44]
TWS	−0.21 [−0.34, −0.08]	−0.14 [−0.31, 0.02]	0.31 [0.14 0.50]
Barystatic	1.00 [0.71, 1.31]	0.80 [0.49, 1.13]	1.97 [1.63 2.33]
Thermosteric	0.52 [0.34, 0.69]	0.71 [0.54, 0.88]	1.19 [0.99 1.44]
Summed contributions	1.52 [1.20, 1.85]	1.51 [1.18, 1.84]	3.16 [2.78 3.57]
Observed GMSL	1.56 [1.24, 1.89]	1.78 [1.48, 2.07]	3.35 [2.91 3.82]
Observed GMSL minus summed contributions	0.04 [−0.31, 0.41]	0.26 [−0.07, 0.59]	0.19 [−0.32 0.70]
Satellite altimetry			3.32 [2.87 3.79]

The numbers in brackets indicate the 90% confidence interval.

impounded, leading to a sea-level drop of 26 ± 9 mm (90% confidence interval), with a peak in dam construction around the 1970s[26]. The rate of global thermosteric sea-level rise since 2000 is significantly greater than at any moment in the twentieth century. However, the barystatic rate since 2000 is not significantly greater than the rate in the 1930s. The only major feature in observed GMSL that is not replicated by the sum of the processes is the low rate in observed sea-level change during the 1920s, although this low rate is found in most ocean basins and is also visible in other reconstructions (Extended Data Fig. 2). A possible explanation for this mismatch could be the low number of available tide-gauge records over the first few decades of data, which results in a less robust reconstruction (Extended Data Fig. 3) and in increasing unquantified uncertainties in individual budget components.

The relative contributions of the barystatic and thermosteric components to GMSL vary over time. Figure 2a shows that the barystatic component dominates over the first half of the twentieth century, explaining more than 80% of total GMSL rise. The barystatic contribution is larger than the thermosteric contribution over most of the second half of the century too, except during the peak of dam construction in the 1970s. Glaciers are the largest contributor to sea-level rise over most of the twentieth century, overtaken by the thermosteric contribution only after 1970. In Fig. 2b, we omit the TWS term to remove the direct anthropogenic contributions due to reservoir impoundment and groundwater depletion. Without the TWS term, the relative contribution from glaciers and ice sheets gradually decreases during the end of the twentieth century; however, their combined contribution increases again from the start of the twenty-first century. This increase

is consistent with recent assessments of the sea-level budget over the satellite era[10].

Basin-mean sea level

The global changes can be broken down into basin-mean changes (Fig. 3, Extended Data Table 1), each with different trends and variability. Although salinity-induced (halosteric) changes in sea level cause negligible changes in GMSL[35], they can be important contributors at the ocean-basin level. Thus, basin-mean changes in sea level due to changes in water density (steric changes) cannot be approximated by thermosteric changes alone[36]. Because in situ salinity estimates before the 1950s are too sparse to extract basin-scale salinity changes, we can assess the basin-mean sea-level budget only since the 1950s.

Over 1957–2018 and 1993–2018, the sea-level budget in each basin is closed within the 90% confidence intervals. The uncertainties of regional sea-level reconstructions vary considerably among basins. This is not only because of differences in tide-gauge coverage (Extended Data Fig. 3), but also to a large extent because of uncertainties in the GIA correction. In some basins, most tide-gauges are located in areas with large GIA uncertainties, such as the northwest Atlantic and the northeast Pacific coasts. On the other hand, the large uncertainties in the South Atlantic can be linked to the low number of tide-gauge records, with only a few records available before the 1960s.

In contrast to the global-mean variability, which is dominated by barystatic variability, basin-mean multidecadal sea-level variability is dominated by steric changes. The steric trends vary considerably between basins: for example, since 1957, the subtropical North Atlantic has experienced a steric trend 2.7 ± 0.4 times higher than the east Pacific. Ocean-mass trends in each basin are more homogeneous, except for the low trend in the subpolar North Atlantic. This low trend is due to the proximity to the Greenland Ice Sheet and regions of substantial glacier mass loss. Owing to GRD effects, oceans near areas of land-mass loss see below-average ocean-mass increases (Extended Data Fig. 4). This below-average increase is partially offset by GIA, which causes an upward trend in this basin. As a result, despite the fact that the observed sea-level changes in the subpolar North Atlantic can be attributed to a different mix of processes, the resulting trend since 1900 is of similar magnitude to the global-mean. GIA also results in above-average sea-level trends in the subtropical North Atlantic; for other basins, its contribution is negligible compared to ocean-mass and steric contributions. In each basin, the trend since 2000 is larger than the trend over the entire period. These high rates of GMSL change since 2000 are seen globally and are not driven by processes limited to a subset of ocean basins.

Conclusions

We reconstructed the GMSL since 1900 and compared it to the sum of the contributing processes. We found that these processes explain the
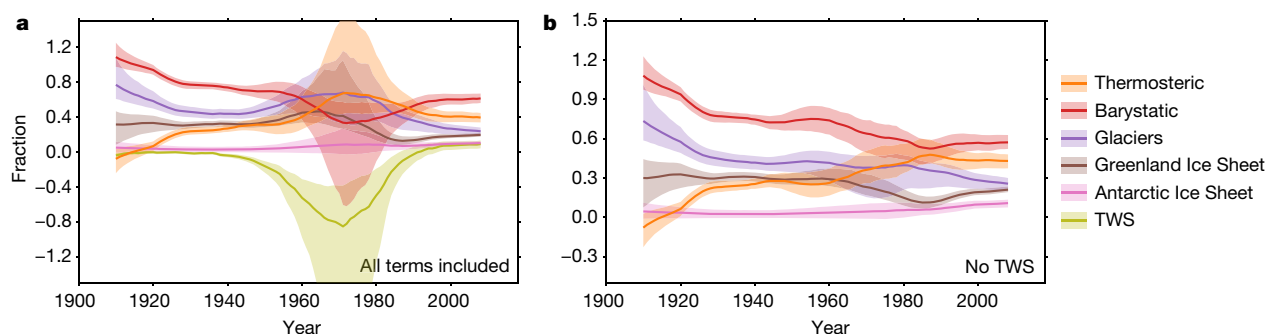
Fig. 2 | Fraction of the 40-year-average summed rate explained by each contributor. a, Fraction with all components included. **b,** Fraction after omitting the TWS component. The shaded regions denote 90% confidence intervals.
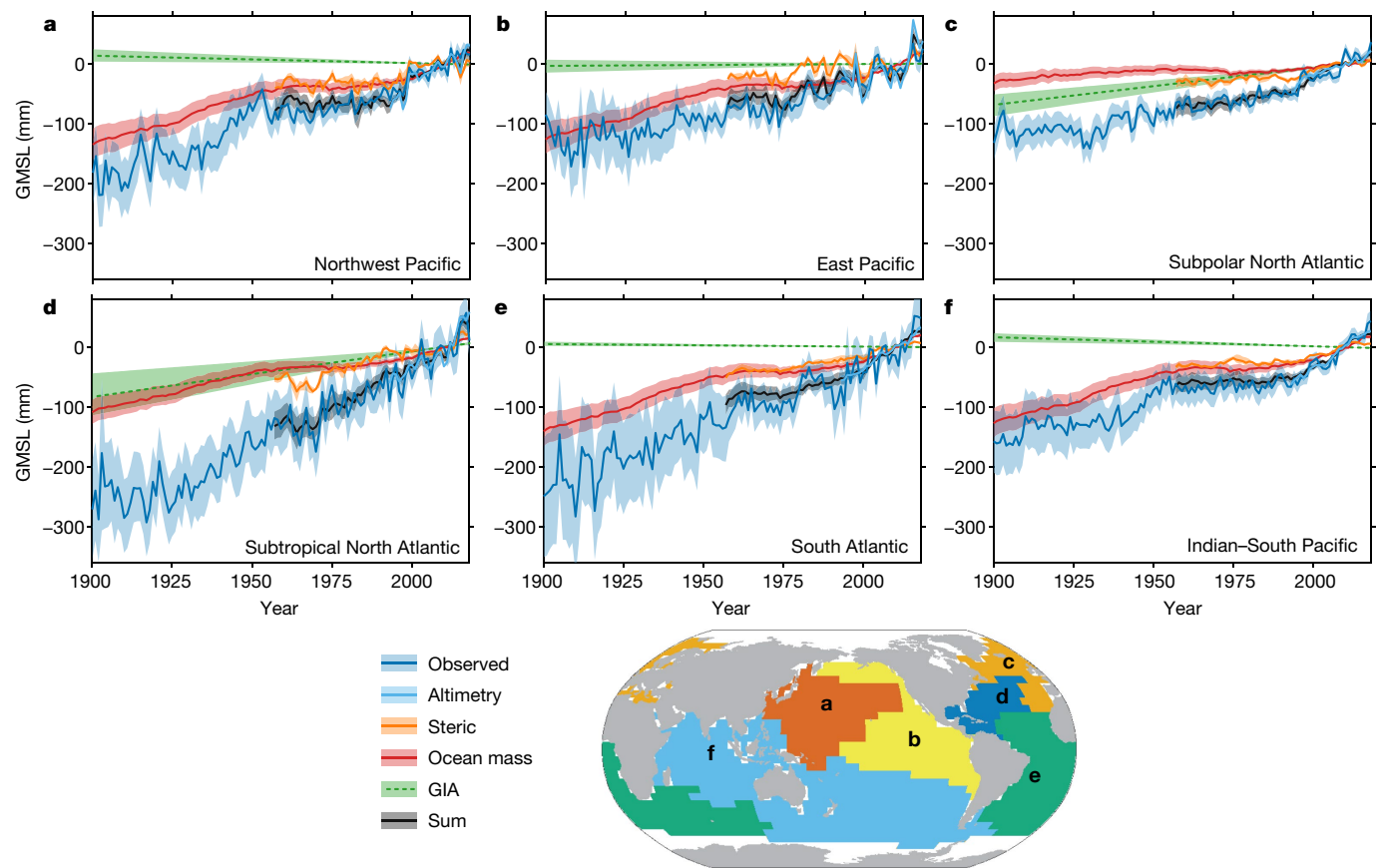
Fig. 3 | Observed basin-mean sea level and contributing processes.
a–**f**, Observed basin-mean sea level, and the estimated contributions and their sum, for the different basins (as indicated on the map). Contrary to the global case, GIA causes basin-mean changes in sea level, and so is included in the sum of contributors. The shaded regions denote the 90% confidence interval. The values are relative to the 2002–2018 mean.

observed twentieth-century GMSL trend and match the multidecadal variability pattern, except for the low rates in observed sea-level rise during the 1920s. Barystatic changes are the primary contributor to sea-level rise, with glacier mass loss being the largest component. Reservoir impoundment caused a substantial, albeit temporary, slowdown of GMSL rise during the 1970s. The relative contributions of thermosteric and barystatic changes to GMSL vary with time. On basin scales, trends and multidecadal variability deviate from the global mean, mostly as a result of variability in the steric component.

In the subpolar North Atlantic, along which almost half of all tide gauges used in this study are located, including many of the longest available records, the ocean-mass contribution over the twentieth century is negligible, whereas GIA causes relative sea level to rise in this basin. This combination results in sea-level trends that are comparable to global-mean trends, but caused by a different combination of processes. Although many of the world's longest tide-gauge records, including the 225-year record from Amsterdam and the 220-year record from Brest, are located along the coast of the subpolar North Atlantic, long-term changes derived from these records are not representative of global-mean changes.

Closure of the twentieth-century sea-level budget, as demonstrated here, implies that no additional unknown processes, such as large-scale deep-ocean thermal expansion or additional mass loss from the Antarctic Ice Sheet, are required to explain the observed changes in global sea level. Such additional processes had been speculated to explain the non-closure found in previous studies of global sea-level budget[2,3,12]. Our demonstration of closure of the global-mean and basin-mean sea-level budget forms a consistent baseline against which process-based and semi-empirical sea-level projections can be benchmarked, without

the need to compare against either the sum of processes or observed sea level[37]. The downward revision of the estimated sea-level rise and updated estimates of the driving processes, particularly the increased estimated glacier mass loss, result in a consistent picture of twentieth-century GMSL rise and its underlying causes.

Online content

Any methods, additional references, Nature Research reporting summaries, source data, extended data, supplementary information, acknowledgements, peer review information; details of author contributions and competing interests; and statements of data and code availability are available at https://doi.org/10.1038/s41586-020-2591-3.

1. Oppenheimer, M. et al. in *IPCC Special Report on the Ocean and Cryosphere in a Changing Climate* (eds Pörtner, H.-O. et al.) Ch.4 (in the press).
2. Moore, J., Jevrejeva, S. & Grinsted, A. The historical global sea-level budget. *Ann. Glaciol.* **52**, 8–14 (2011).
3. Gregory, J. M. et al. Twentieth-century global-mean sea level rise: is the whole greater than the sum of the parts? *J. Clim.* **26**, 4476–4499 (2013).
4. Hay, C. C., Morrow, E., Kopp, R. E. & Mitrovica, J. X. Probabilistic reanalysis of twentieth-century sea-level rise. *Nature* **517**, 481–484 (2015); erratum **552**, 278 (2017).
5. Dangendorf, S. et al. Persistent acceleration in global sea-level rise since the 1960s. *Nat. Clim. Change* **9**, 705–710 (2019).
6. Chambers, D. P., Merrifield, M. A. & Nerem, R. S. Is there a 60-year oscillation in global mean sea level? *Geophys. Res. Lett.* **39**, L18607 (2012).
7. Munk, W. Twentieth century sea level: an enigma. *Proc. Natl Acad. Sci. USA* **99**, 6550–6555 (2002).
8. Church, J. A. et al. Revisiting the Earth's sea-level and energy budgets from 1961 to 2008. *Geophys. Res. Lett.* **38**, L18601 (2011); erratum **40**, 4066 (2013).
9. Frederikse, T., Jevrejeva, S., Riva, R. E. M. & Dangendorf, S. A consistent sea-level reconstruction and its budget on basin and global scales over 1958–2014. *J. Clim.* **31**, 1267–1280 (2018).

10. WCRP Global Sea Level Budget Group. Global sea-level budget 1993–present. *Earth Syst. Sci. Data* **10**, 1551–1590 (2018).

11. Cabanes, C. Sea level rise during past 40 years determined from satellite and in situ observations. *Science* **294**, 840–842 (2001).

12. Miller, L. & Douglas, B. C. Mass and volume contributions to twentieth-century global sea level rise. *Nature* **428**, 406–409 (2004).

13. Jevrejeva, S., Matthews, A. & Slangen, A. The twentieth-century sea level budget: recent progress and challenges. *Surv. Geophys.* **38**, 295–307 (2017).

14. Kjeldsen, K. K. et al. Spatial and temporal distribution of mass loss from the Greenland Ice Sheet since ad 1900. *Nature* **528**, 396–400 (2015).

15. Zanna, L., Khatiwala, S., Gregory, J. M., Ison, J. & Heimbach, P. Global reconstruction of historical ocean heat storage and transport. *Proc. Natl Acad. Sci. USA* **116**, 1126–1131 (2019).

16. Parkes, D. & Marzeion, B. Twentieth-century contribution to sea-level rise from uncharted glaciers. *Nature* **563**, 551–554 (2018).

17. Humphrey, V. & Gudmundsson, L. GRACE-REC: a reconstruction of climate-driven water storage changes over the last century. *Earth Syst. Sci. Data* **11**, 1153–1170 (2019).

18. Marzeion, B., Leclercq, P. W., Cogley, J. G. & Jarosch, A. H. Brief Communication: Global reconstructions of glacier mass change during the 20th century are consistent. *Cryosphere* **9**, 2399–2404 (2015).

19. Cheng, L., Abraham, J., Hausfather, Z. & Trenberth, K. E. How fast are the oceans warming? *Science* **363**, 128–129 (2019).

20. Dangendorf, S. et al. Reassessment of 20th century global mean sea level rise. *Proc. Natl Acad. Sci. USA* **114**, 5946–5951 (2017).

21. Zemp, M. et al. Global glacier mass changes and their contributions to sea-level rise from 1961 to 2016. *Nature* **568**, 382–386 (2019); erratum **577**, E9 (2020).

22. Adhikari, S. et al. What drives 20th century polar motion? *Earth Planet. Sci. Lett.* **502**, 126–132 (2018).

23. The IMBIE team. Mass balance of the Antarctic Ice Sheet from 1992 to 2017. *Nature* **558**, 219–222 (2018).

24. Bamber, J. L., Westaway, R. M., Marzeion, B. & Wouters, B. The land ice contribution to sea level during the satellite era. *Environ. Res. Lett.* **13**, 063008 (2018); corrigendum **13**, 099502 (2018).

25. Mouginot, J. et al. Forty-six years of Greenland Ice Sheet mass balance from 1972 to 2018. *Proc. Natl Acad. Sci. USA* **116**, 9239–9244 (2019).

26. Chao, B. F., Wu, Y. H. & Li, Y. S. Impact of artificial reservoir water impoundment on global sea level. *Science* **320**, 212–214 (2008).

27. Döll, P., Müller Schmied, H., Schuh, C., Portmann, F. T. & Eicker, A. Global-scale assessment of groundwater depletion and related groundwater abstractions: combining hydrological modeling with information from well observations and GRACE satellites. *Wat. Resour. Res.* **50**, 5698–5720 (2014).

28. Wada, Y. et al. Fate of water pumped from underground and contributions to sea-level rise. *Nat. Clim. Change* **6**, 777–780 (2016).

29. Watkins, M. M., Wiese, D. N., Yuan, D.-N., Boening, C. & Landerer, F. W. Improved methods for observing Earth's time variable mass distribution with GRACE using spherical cap mascons. *J. Geophys. Res. Solid Earth* **120**, 2648–2671 (2015).

30. Levitus, S. et al. World ocean heat content and thermosteric sea level change (0–2000 m), 1955–2010. *Geophys. Res. Lett.* **39**, L10603 (2012).

31. Ishii, M. et al. Accuracy of global upper ocean heat content estimation expected from present observational data sets. *Sci. Online Lett. Atmos.* **13**, 163–167 (2017).

32. Cheng, L. & Zhu, J. Benefits of CMIP5 multimodel ensemble in reconstructing historical ocean subsurface temperature variations. *J. Clim.* **29**, 5393–5416 (2016).

33. Thompson, P. R., Hamlington, B. D., Landerer, F. W. & Adhikari, S. Are long tide gauge records in the wrong place to measure global mean sea level rise? *Geophys. Res. Lett.* **43**, 10403–10411 (2016).

34. Beckley, B. D., Callahan, P. S., Hancock, D. W., Mitchum, G. T. & Ray, R. D. On the "cal-mode" correction to TOPEX satellite altimetry and its effect on the global mean sea level time series. *J. Geophys. Res. Oceans* **122**, 8371–8384 (2017).

35. Gregory, J. M. et al. Concepts and terminology for sea level: mean, variability and change, both local and global. *Surv. Geophys.* **40**, 1251–1289 (2019).

36. Durack, P. J., Wijffels, S. E. & Gleckler, P. J. Long-term sea-level change revisited: the role of salinity. *Environ. Res. Lett.* **9**, 114017 (2014).

37. Mengel, M. et al. Future sea level rise constrained by observations and long-term commitment. *Proc. Natl Acad. Sci. USA* **113**, 2597–2602 (2016).

Article

Methods

The global-mean and basin-mean sea-level changes that we report are relative sea-level (RSL) changes[35], corresponding to the total change in sea-water volume. RSL changes are changes relative to the underlying seafloor. They differ from geocentric sea-level changes observed by satellite altimetry, owing to seafloor deformation. We divide the global ocean into six basins[38]. These basins (Extended Data Fig. 3) are defined using a clustering approach that merges locations that share a common interannual sea-level variability signal, as observed by satellite altimetry. We define the global ocean as the sum of all basins. Our basins do not cover the highest latitudes of polar oceans, as satellites cannot sufficiently provide data for these regions. Sea-level changes in these regions, which cover 7% of the total ocean area, are not included. Because the omitted area is small, only a large local anomaly in sea-level rise would have to potential to affect GMSL substantially. A recent sea-level reconstruction[5] estimates a rate of sea-level rise of 1.0 ± 0.8 mm yr^{-1} in the Arctic ocean and a rate of 1.6 ± 0.6 mm yr^{-1} in the Southern Ocean over 1900–2015. Using these rates to extend our reconstruction has a negligible (less than 0.1 mm yr^{-1}) effect on the global-mean sea-level trend. Therefore, omitting these oceans when reconstructing global-mean sea-level changes is unlikely to cause substantial GMSL changes.

The ensemble approach

Assessing closure of the global-mean and basin-mean sea-level budget requires an estimate of the mean and associated uncertainties of the observed sea-level changes, as well as those of the major contributing processes. Some processes, especially GIA, affect both the sea-level observations and estimates of the contributing processes, and the reconstructed sea-level changes and the sum of processes are not fully independent. Therefore, we use a Monte Carlo approach to obtain a consistent set of observed sea level, its contributing processes and associated uncertainties. We generate 5,000 realizations of observed sea level and the contributing processes. For each process, we use one of the two following approaches. If a large number of estimates is available, we randomly select one estimate (for example, GIA). If only a single or limited number of independent estimates are available (for example, glacier mass loss), we generate ensemble members by randomly selecting and perturbing one of these estimates. We perturb the estimate by drawing random numbers from a Gaussian distribution using the a priori uncertainty of that estimate as the standard deviation and adding these random numbers to the estimate. We compute basin-mean and global-mean sea-level changes and the contributing processes for each ensemble member. This procedure provides 5,000 realizations of global-mean and basin-mean sea level, all components, and the difference between sea level and the sum of the components, in which all known sources of uncertainty and the spread among different estimates have been propagated. We compute all the time series, moving trends and linear trends for each ensemble member and subsequently derive the mean and confidence intervals from the ensemble. This procedure ensures that the underlying co-variances between the sea-level observations and contributing processes are propagated into the final estimates. Extended Data Fig. 1 shows the procedure that is followed for each individual ensemble member. In the sections below, we describe the data and estimates used for reconstructing sea level and each process.

GIA

While not changing contemporary GMSL, GIA causes changes in the Earth's gravity field and the shape of the solid Earth, and changes local relative sea level. These changes affect observations from tide gauges, altimetry, GNSS stations and our estimates of the contributors to barystatic sea-level changes[39]. Estimates of GIA-induced changes in sea level, gravity and the solid Earth all come with a substantial uncertainty.

Because GIA input parameters simultaneously affect several components of the sea-level budget, these components and their uncertainties are not fully independent of each other[39,40]. To estimate the GIA effects and to propagate the mutually dependent uncertainties in the GIA predictions into all affected observations, we use an ensemble of GIA estimates[41]. This study[41] provides a 128,000-member ensemble of GIA predictions, computed by varying solid-Earth parameters (lithosphere thickness and mantle viscosities) and amplitudes of global deglaciation histories over the past 20,000 years. Each GIA ensemble member provides a consistent set of changes in relative sea level, solid-Earth deformation and changes in equivalent water height, used to correct GRACE observations, and comes with a likelihood that reflects how good the fit is to a dataset of vertical GNSS velocities and palaeo sea-level records. Therefore, this model allows for a robust quantification of the uncertainties associated with GIA. The spread between the ensemble members depicts the uncertainty in the GIA predictions due to uncertainty in the solid-Earth parameters and the deglaciation history. Large uncertainties can therefore be found around the edges of formerly glaciated regions, such as the coastlines of Alaska and Fennoscandia, and the forebulge collapse regions along the North American coastlines. The ensemble approach ensures that these uncertainties are propagated into estimates of basin-mean and global-mean sea level. See ref. [41] for further details about the GIA predictions and the data used to weigh the GIA ensemble members. For each of our ensemble members, we randomly select one GIA prediction from the 128,000-member ensemble. Extended Data Fig. 4b shows the ensemble-mean RSL changes caused by GIA. Using the ICE6G D (VM5a) model[42] to account for GIA (Extended Data Fig. 5) does not cause noteworthy differences in global-mean and basin-mean observed sea level and the contributing processes. The differences in the subtropical North Atlantic basin are slightly larger (up to 0.3 mm yr^{-1}), but even here the GIA-related sea-level changes are within the confidence intervals of our GIA ensemble.

Contemporary mass redistribution

For the sea-level changes due to contemporary mass redistribution, we need to estimate the amount of water that is redistributed, and where on land the water is added or removed. During 2003–2018, we use GRACE and GRACE-FO observations, based on the JPL RL06 mascon solution[29,43,44]. This solution provides monthly land-mass changes on a nominal 3-degree grid, from which we compute annual averages. Each grid cell has an associated measurement uncertainty, based on the formal error covariance matrix of the GRACE solution[43]. For each ensemble member, we randomly draw from these uncertainty estimates, perturb the mass estimates with this draw and correct for GIA. We then split the land-mass changes from GRACE into mass changes from glaciers, ice sheets and TWS using a previously described method[45].

Over 1900–2003, we use multiple estimates of each of the aforementioned processes. To combine these estimates with the GRACE observations, we average all observation-based mass-loss estimates over the same grid as the GRACE observations and remove the common mean in 2003 at every GRACE grid cell. Extended Data Fig. 6 shows all individual estimates and the resulting final composite estimate for each mass-redistribution process.

For glaciers, we use two mass-change estimates. The first estimate, which covers the whole twentieth century, is based on a global glacier model that is driven by observation-based surface forcing[18]. This model produces estimates of the annual rate of glacier mass loss for each of the 19 glaciated regions defined in the Randolph Glacier Inventory (RGI)[46]. The second estimate[21], which provides mass changes since 1961, uses in situ glaciological and geodetic observations to derive total mass changes for each glaciated region. Both estimates provide uncertainties of the rate. For each ensemble member, we randomly choose between the two estimates. Before 1961, each member uses the estimates from the first estimate. Both estimates provide annual rate

uncertainties. We draw random numbers using the rate uncertainties as the standard deviation, add them to the estimated rate and integrate this perturbed rate to obtain the total glacier mass changes. Because GRACE cannot distinguish the contributions from the Greenland and Antarctic peripheral glaciers from those from the ice sheets, we do not include these glaciers into the glacier mass balance. For Greenland, we add the peripheral glaciers to the ice-sheet contribution. For Antarctica, the mass balance of its peripheral glaciers is very uncertain, owing to the lack of observations[47]. However, since 2003, only a very small mass loss has been observed for these glaciers[48], and observations since the 1950s do not suggest a large contribution[21]. Therefore, we assume no mass loss from the Antarctic peripheral glaciers. We account for missing (owing to their relatively small size) and disappeared glaciers using a previous estimate[16]. This study[16] provides upper- and lower-bound estimates of the contribution of missing and disappeared glaciers. For each ensemble member, we uniformly sample between the upper- and lower-bound estimates. Since this estimate does not provide glacier mass changes per RGI region, we assume that the regional distribution of the contribution from missing and disappearing glaciers can be scaled by the regional relative contribution from the large glaciers as recognized by RGI.

For the Greenland Ice Sheet, we use three estimates: a mass-balance reconstruction[14] that covers 1900–2003, input–output estimates[25] that cover 1972–2003, and a multi-method assessment[24] that covers 1993–2003. For each ensemble member, we randomly select one of these models. We use the first estimate for the contribution over the era for which the others do not provide an estimate. Each estimate provides a rate uncertainty, and we use these uncertainties to generate a perturbed estimate for each ensemble member using the same procedure as for glaciers. These reconstructions (except the one from ref. [24]) do not include the contribution from peripheral glaciers. For these estimates, we add the estimated peripheral glacier contribution to the Greenland mass balance using the same approach as for other glaciated regions.

For Antarctica, no mass-balance reconstruction exists before the satellite era, although observational evidence suggests twentieth-century mass loss, especially from West Antarctica[49,50]. Therefore, we assume a small Antarctic Ice Sheet contribution before 1993 of 0.05 ± 0.04 mm yr^{-1}, based on an existing compilation[22]. For 1993–2003, we use the multi-method assessments[23,24] to derive the mass changes. To obtain an estimate of the spatial pattern of the mass changes from both ice sheets, we derive the spatial pattern of the mass loss from the perturbed GRACE observations. We assume this spatial pattern remains constant in time.

The TWS component consists of natural and anthropogenic processes. For natural TWS, we use a twentieth-century reconstruction[17] that provides 100 ensemble members of natural TWS changes. We mask out all glacier and ice-sheet regions from these estimates, and randomly select one of the 100 TWS ensemble members. For anthropogenic TWS changes, we consider artificial reservoir impoundment and groundwater depletion. For reservoir impoundment, we use an updated list of global artificial reservoirs[26] and the ICOLDS dam database[51]. We assume the filling and seepage rates of each reservoir follow previous estimates[26]. The ICOLDS dam database, which covers 93% of the total impounded volume, provides location coordinates of each reservoir; the database from ref. [26] does not. To approximate the regional distribution of this reservoir impoundment, we add the impounded water of the reservoirs with unknown location to the reservoirs with known location. We compute the fraction of the total impounded volume held by each known reservoir, and distribute the water from reservoirs with unknown location using this fraction. To our knowledge, for reservoir impoundment, no formal uncertainties have been quantified. Likely sources of the uncertainty in the reservoir impoundment stem from reservoir filling levels, storage-capacity loss due to sedimentation and seepage effects[3,52]. Previous assessments assumed rates of uncertainties of 10%–30%[8,28]; we assume an uncertainty of 20% (1σ).

For groundwater depletion, we use two gridded depletion estimates. Ref. [53] provides depletion estimates over 1900–2003. However, a substantial fraction of the depleted groundwater remains on land rather than ending up in the ocean[28]. To account for this effect, we assume that 40% of the depleted groundwater stays on land, and we scale the estimated depletion from this study by a factor of 0.6 (ref. [54]). We also use depletion estimates[27] over 1961–2003. Similarly to the glacier and ice-sheet case, we randomly select one of the estimates for each ensemble member. We assume an uncertainty of 20% (1σ) in groundwater depletion, which corresponds to previously estimated uncertainties[28].

These land-mass changes result in barystatic sea-level changes and, owing to GRD effects, in regionally varying sea-level change and solid-Earth deformation patterns. For each ensemble member, we solve the sea-level equation using a pseudo-spectral method[55,56]. The spherical-harmonics transformations are computed using the SHTns library[57] up to degree and order 360. The resulting geoid changes and deformation are expressed relative to the centre-of-mass reference frame, and include rotational feedback[58]. We assume an elastic solid-Earth response to the land-mass changes, for which we use Love numbers based on[59] the Preliminary Referenced Earth Model[60]. With this procedure, we obtain 5,000 ensemble members, each consisting of annual time series of local sea-level changes and solid-Earth deformation due to contemporary mass redistribution. Extended Data Fig. 4a, c, e shows the ensemble-mean RSL trends due to contemporary mass redistribution.

Steric changes
We estimate global-mean and basin-mean steric changes for 1957–2018 from gridded temperature and salinity reconstructions based on in situ observations of temperature and salinity. We use existing gridded estimates[31,32] for the upper 2,000 m. From these observations, we compute steric height anomalies using the TEOS-10 GSW software[61]. We also use gridded steric sea-level change estimates[30]. For each ensemble member, one of these estimates is selected randomly. Before the end of the 1950s, in situ observations are too sparse to derive unbiased steric changes[62]. For the upper-ocean (above 2,000 m) contribution before 1957, we use estimates[15] computed from sea-surface temperature anomaly observations and estimates of ocean heat anomaly pathways from an ocean reanalysis. We also use the deep-ocean (below 2,000 m) steric expansion[15] for the full 1900–2018 period. These estimates come with an uncertainty, which is used to perturb each ensemble member. In the Argo float data, a salinity drift has been detected since 2015[63], which causes an underestimation of global steric sea level. We correct for this drift by removing the estimated global-mean halosteric sea-level changes from each gridded estimate. Extended Data Fig. 7 depicts the time series of the individual steric products and the resulting estimates used in this paper.

Sea-level observations
We use annual-mean tide-gauge observations from the revised local reference (RLR) dataset from the Permanent Service for Mean Sea Level[64,65], as well as an extended tide-gauge dataset[66], which has been updated until 2018. We remove observations that have been flagged for quality issues. Some stations show apparent data problems, such as spikes, jumps, drifts and large trends. These problems are typically caused by earthquakes, local subsidence, levelling issues and instrument problems. Owing to the multitude of the data problems, such stations cannot be automatically flagged and excluded, on the basis of pre-set criteria, and we manually remove these regions from the analysis. We ultimately use 559 individual tide-gauge records in our reconstruction. From each sea-level record, we remove the self-consistent equilibrium nodal cycle[67] and the effects of local wind and sea-level pressure changes. To this end, we use wind and sea-level pressure fields from the ERA-20c reanalysis[68] over 1900–1979 and ERA5 reanalysis[69] from 1979–2018, and use a simple linear regression model to remove

Article

the wind and pressure effects[70]. Some locations, such as Aberdeen, Sydney and Singapore, have multiple tide-gauge records with different observational periods. We merge stations that are within 20 km of each other and have an overlap of at least 5 station years into regions. Henceforth, we refer to regions to denote any location that has a single or multiple merged tide-gauge observations. We only consider regions with at least 20 years of data. We link each region to a single ocean basin. All regions and the associated basins are shown in Extended Data Fig. 3.

VLM

Tide-gauge observations are affected by VLM[71], and correcting these records for VLM has resulted in more coherent sea-level trends across different tide gauges[20,72]. We use VLM observations from permanent GNSS stations and from the difference between satellite-altimetry and tide-gauge observations[71,73]. The RSL patterns associated with GIA and GRD are partially caused by solid-Earth deformation, which is observed as VLM. To avoid double-counting, we subtract the modelled solid-Earth deformation that results from GIA (R_{GIA}) and contemporary GRD (R_{GRD}) from the observed VLM time series (R_{obs}), to obtain a time series of residual VLM[9,45]:

$$R_{residual}(t) = R_{obs}(t) - R_{GIA}(t) - R_{GRD}(t) \qquad (1)$$

We compute the linear trend in residual VLM, and we assume that the rate of residual VLM is representative for the full length of the tide-gauge record.

We use the GNSS station database from the University of Nevada, Reno[74]. We select all GNSS stations that are within a 30-km radius of each region, have at least 4 years of daily observations, and for which the standard error of the residual VLM trend does not exceed 1 mm yr^{-1}. We estimate the residual VLM trend using the MIDAS trend estimator[75]. We compute residual VLM for each ensemble member. The uncertainty in the derived trend is caused by the uncertainty in the corrections for GIA and contemporary GRD effects, and by the uncertainty that arises from estimating a linear trend from serially correlated data. The uncertainty due to GIA and contemporary GRD is estimated by computing the residual VLM trend for each individual ensemble member. To account for serial correlation, for each ensemble member we determine the trend uncertainty provided by the MIDAS trend estimator. We then draw a random number from a Gaussian distribution with this trend uncertainty as standard deviation, and perturb the estimated trend with this random number.

To obtain residual VLM trends from the difference between satellite-altimetry and tide-gauge observations, we use the MEaSUREs gridded sea surface height anomalies version 1812 dataset[76]. This dataset has been corrected for calibration issues that caused a sea-level drift over the first years of the altimetry era[34]. The altimetry data covers the period 1993–2018. To obtain local residual VLM, we subtract GIA and contemporary GRD effects from altimetry. We require 15 years of overlap between altimetry and the tide gauge, and select all grid points within a 300-km radius for which the correlation between annual-mean de-trended altimetry and tide-gauge sea level is above 0.5. This value, and the radius of 300 km, are chosen as a compromise between accuracy and the number of locations for which VLM can be estimated[73]. We compute the residual VLM time series for each accepted altimetry grid point, and then compute the mean residual VLM time series by taking the mean of all individual time series, weighted by the correlation with the tide-gauge record. From this time series, we compute the linear trend and standard error by assuming that the serial correlation of the time series can be approximated by a first-order autoregressive process. This computation is performed using the Hector software[77]. For stations for which no single altimetry grid point has a correlation of 0.5 or higher, or for which the standard error is above 1 mm yr^{-1}, no VLM estimate is generated. Similarly to the GNSS approach, we perturb

each ensemble member with the trend uncertainty that arises from serial correlation in the time series.

Some VLM observations appear as single outliers compared to nearby other observations, or result in unrealistically high or low sea-level trends. As for the tide-gauge selection procedure, owing to the multitude of possible problems in VLM estimates, no general criteria can be applied to catch these problems. Therefore, we manually remove VLM estimates that show such problems. For regions with multiple GNSS stations, or with both GNSS and altimetry VLM estimates available, we use the average residual VLM trend, weighted by the inverse of the squared standard errors of the individual estimates. We are not able to estimate a VLM trend for all tide-gauge regions. For stations for which no VLM trend is available, we assume no residual VLM and a residual VLM standard error of 1 mm yr^{-1}. This standard error is based on the maximum VLM uncertainty that we accept and on the standard deviation among the residual VLM estimates, 1.5 mm yr^{-1}. In some regions, large sea-level trends are compensated for by large residual VLM trends. As a result, this standard deviation is probably biased high for regions without residual VLM estimates, because regions with a large sea-level trend and no residual VLM estimate are removed during the quality control phase.

Global-mean and basin-mean sea-level reconstruction

Following ref. [9], before merging the individual region estimates into basin-mean curves, we estimate and remove the biases between local sea-level changes in each region and basin-mean sea-level changes that result from GIA, contemporary GRD effects and residual VLM. This correction results in an estimate of basin-mean sea level (η_{basin}), given observed regional sea level (η_{region}), the difference between regional sea-level changes that result from GIA ($\eta_{GIA,region}$) and GRD ($\eta_{GRD,region}$), and the associated basin-mean sea-level changes, as well as residual VLM:

$$\eta_{basin}(t) = \eta_{region}(t) + [\eta_{GIA,basin}(t) - \eta_{GIA,region}(t)] \\ + [\eta_{GRD,basin}(t) - \eta_{GRD,region}(t)] + R_{residual}(t) \qquad (2)$$

Local sea-level variability may not be representative for the basin as a whole. To assess the uncertainty due to this non-representativeness, we perturb each ensemble member of the sea-level observations $\eta_{region}(t)$ from each individual region with a realization of first-order autoregressive (AR1) noise. The AR1 noise parameters are computed from the standard deviation and the first-order serial correlation of the regional sea-level observations. After computing all basin sea-level estimates from each individual region, we merge all the individual regions into a single basin estimate using the virtual-station method[9,20,78], in which the two nearest regions are merged into a new virtual station halfway between the merged stations. Tide-gauge observations are not tied to a common vertical datum system. To account for different datum systems during the averaging process, we remove the common mean between two series estimated over their overlapping period. This procedure is repeated until one virtual station is left. The sea-level change estimate from the final virtual station is used as the basin-mean estimate. We obtain the final GMSL estimate by averaging the basin-mean estimates, weighted by the relative surface area of each basin.

The resulting GMSL estimate shows a linear trend and multidecadal variability pattern that agree with other recent reconstructions[4,5,20]. These recent reconstructions all show lower twentieth-century rates than do earlier assessments[79,80], as shown in Extended Data Fig. 2.

The global-mean and basin-mean altimetry curves are computed using the same gridded altimetry product as used for the VLM computations. To obtain basin-mean and global-mean RSL, we add the modelled deformation of the seafloor due to GIA and contemporary GRD effects to the altimetry curves[81].

The linear trends and accompanying uncertainty estimates in all basin-mean and global-mean quantities discussed here are computed from the linear trends in each ensemble member. Because the unique

GIA model used in each ensemble member has an associated likelihood, we use the likelihood from the GIA model as the weight for the ensemble member when computing the mean and confidence intervals in all components. Because not all terms follow a Gaussian distribution, the confidence intervals are not assumed to be symmetric, and we directly compute the confidence intervals from the 5th and 95th percentile of the weighted ensemble. We account for the uncertainties due to serial correlation in the time series by adding the estimated trend uncertainty to the ensemble spread in quadrature. We assume that the spectrum of all time series can be approximated by a generalized Gauss–Markov spectrum[82]. We compute the noise parameters and the resulting trend uncertainty using the Hector software[77].

Data availability

The resulting global and basin-scale reconstructions, the time series of global and basin sea-level changes and its contributors, grids with local sea-level and solid-Earth deformation due to contemporary GRD effects, and the individual ensemble members are available at https://doi.org/10.5281/zenodo.3862995.

Code availability

The codes to compute the ensemble of observed sea-level changes and contributing processes, and the post-processing routines to compute statistics and to generate the figures are available at https://github.com/thomasfrederikse/sealevelbudget_20c.

38. Thompson, P. R. & Merrifield, M. A. A unique asymmetry in the pattern of recent sea level change. *Geophys. Res. Lett.* **41**, 7675–7683 (2014).
39. Tamisiea, M. E. Ongoing glacial isostatic contributions to observations of sea level change. *Geophys. J. Int.* **186**, 1036–1044 (2011).
40. Melini, D. & Spada, G. Some remarks on glacial isostatic adjustment modelling uncertainties. *Geophys. J. Int.* **218**, 401–413 (2019).
41. Caron, L. et al. GIA model statistics for GRACE hydrology, cryosphere, and ocean science. *Geophys. Res. Lett.* **45**, 2203–2212 (2018).
42. Peltier, W. R., Argus, D. F. & Drummond, R. Comment on "An assessment of the ICE-6G_C (VM5a) glacial isostatic adjustment model" by Purcell et al. *J. Geophys. Res. Solid Earth* **123**, 2019–2028 (2018).
43. Wiese, D. N., Landerer, F. W. & Watkins, M. M. Quantifying and reducing leakage errors in the JPL RL05M GRACE mascon solution. *Wat. Resour. Res.* **52**, 7490–7502 (2016).
44. Loomis, B. D., Rachlin, K. E., Wiese, D. N., Landerer, F. W. & Luthcke, S. B. Replacing GRACE/GRACE-FO C_{30} with satellite laser ranging: impacts on Antarctic Ice Sheet mass change. *Geophys. Res. Lett.* **47**, e2019GL085488 (2020).
45. Frederikse, T., Landerer, F. W. & Caron, L. The imprints of contemporary mass redistribution on local sea level and vertical land motion observations. *Solid Earth* **10**, 1971–1987 (2019).
46. Pfeffer, W. T. et al. The Randolph Glacier Inventory: a globally complete inventory of glaciers. *J. Glaciol.* **60**, 537–552 (2014).
47. Marzeion, B., Jarosch, A. H. & Hofer, M. Past and future sea-level change from the surface mass balance of glaciers. *Cryosphere* **6**, 1295–1322 (2012).
48. Gardner, A. S. et al. A reconciled estimate of glacier contributions to sea level rise: 2003 to 2009. *Science* **340**, 852–857 (2013).
49. Cook, A. J., Fox, A. J., Vaughan, D. G. & Ferrigno, J. G. Retreating glacier fronts on the Antarctic peninsula over the past half-century. *Science* **308**, 541–544 (2005).
50. Smith, J. A. et al. Sub-ice-shelf sediments record history of twentieth-century retreat of Pine Island Glacier. *Nature* **541**, 77–80 (2017).
51. Lehner, B. et al. High-resolution mapping of the world's reservoirs and dams for sustainable river-flow management. *Front. Ecol. Environ.* **9**, 494–502 (2011).
52. Lettenmaier, D. P. & Milly, P. C. D. Land waters and sea level. *Nat. Geosci.* **2**, 452–454 (2009).
53. Wada, Y. et al. Past and future contribution of global groundwater depletion to sea-level rise. *Geophys. Res. Lett.* **39**, L09402 (2012).
54. Wada, Y. et al. Recent changes in land water storage and its contribution to sea level variations. *Surv. Geophys.* **38**, 131–152 (2017).
55. Tamisiea, M. E. et al. Impact of self-attraction and loading on the annual cycle in sea level. *J. Geophys. Res.* **115**, C07004 (2010).
56. Adhikari, S., Ivins, E. R., Frederikse, T., Landerer, F. W. & Caron, L. Sea-level fingerprints emergent from GRACE mission data. *Earth Syst. Sci. Data* **11**, 629–646 (2019).
57. Schaeffer, N. Efficient spherical harmonic transforms aimed at pseudospectral numerical simulations. *Geochem. Geophys. Geosyst.* **14**, 751–758 (2013).
58. Milne, G. A. & Mitrovica, J. X. Postglacial sea-level change on a rotating Earth. *Geophys. J. Int.* **133**, 1–19 (1998).
59. Wang, H. et al. Load Love numbers and Green's functions for elastic Earth models PREM, iasp91, ak135, and modified models with refined crustal structure from Crust 2.0. *Comput. Geosci.* **49**, 190–199 (2012).
60. Dziewonski, A. M. & Anderson, D. L. Preliminary reference Earth model. *Phys. Earth Planet. Inter.* **25**, 297–356 (1981).
61. McDougall, T. J. & Barker, P. M. *Getting Started with TEOS-10 and the Gibbs Seawater (GSW) Oceanographic Toolbox* (SCOR/IAPSO WG127, 2011).
62. Cheng, L. et al. Improved estimates of ocean heat content from 1960 to 2015. *Sci. Adv.* **3**, e1601545 (2017).
63. Roemmich, D. et al. On the future of Argo: a global, full-depth, multi-disciplinary array. *Front. Mar. Sci.* **6**, 439 (2019).
64. Holgate, S. J. et al. New data systems and products at the permanent service for mean sea level. *J. Coast. Res.* **29**, 493–504 (2013).
65. Permanent Service for Mean Sea Level (PSMSL). *Tide Gauge Data* (retrieved 29 April 2019); http://www.psmsl.org/data/obtaining/.
66. Hogarth, P. Preliminary analysis of acceleration of sea level rise through the twentieth century using extended tide gauge data sets (August 2014). *J. Geophys. Res. Oceans* **119**, 7645–7659 (2014).
67. Woodworth, P. L. A note on the nodal tide in sea level records. *J. Coast. Res.* **280**, 316–323 (2012).
68. Poli, P. et al. ERA-20C: an atmospheric reanalysis of the twentieth century. *J. Clim.* **29**, 4083–4097 (2016).
69. Copernicus Climate Change Service (C3S). *ERA5: Fifth Generation of ECMWF Atmospheric Reanalyses of the Global Climate* (2019); https://doi.org/10.24381/cds.f17050d7.
70. Frederikse, T. & Gerkema, T. Multi-decadal variability in seasonal mean sea level along the North Sea coast. *Ocean Sci.* **14**, 1491–1501 (2018).
71. Wöppelmann, G. & Marcos, M. Vertical land motion as a key to understanding sea level change and variability. *Rev. Geophys.* **54**, 64–92 (2016).
72. Wöppelmann, G. et al. Evidence for a differential sea level rise between hemispheres over the twentieth century. *Geophys. Res. Lett.* **41**, 1639–1643 (2014).
73. Kleinherenbrink, M., Riva, R. & Frederikse, T. A comparison of methods to estimate vertical land motion trends from GNSS and altimetry at tide gauge stations. *Ocean Sci.* **14**, 187–204 (2018).
74. Blewitt, G., Hammond, W. & Kreemer, C. Harnessing the GPS data explosion for interdisciplinary science. *Eos* **99**, https://doi.org/10.1029/2018EO104623 (2018).
75. Blewitt, G., Kreemer, C., Hammond, W. C. & Gazeaux, J. MIDAS robust trend estimator for accurate GPS station velocities without step detection. *J. Geophys. Res. Solid Earth* **121**, 2054–2068 (2016).
76. Zlotnicki, V., Qu, Z. & Willis, J. *MEaSUREs Gridded Sea Surface Height Anomalies Version 1812* (PODAAC, 2019); https://doi.org/10.5067/SLREF-CDRV2.
77. Bos, M. S., Fernandes, R. M. S., Williams, S. D. P. & Bastos, L. Fast error analysis of continuous GNSS observations with missing data. *J. Geod.* **87**, 351–360 (2013).
78. Jevrejeva, S., Moore, J., Grinsted, A., Matthews, A. & Spada, G. Trends and acceleration in global and regional sea levels since 1807. *Global Planet. Change* **113**, 11–22 (2014).
79. Church, J. A. & White, N. J. Sea-level rise from the late 19th to the early 21st century. *Surv. Geophys.* **32**, 585–602 (2011).
80. Church, J. et al. in *Climate Change 2013: The Physical Science Basis. Contribution of Working Group I to the Fifth Assessment Report of the Intergovernmental Panel on Climate Change* (eds Stocker, T. et al.) Ch. 13, 1137–1216 (Cambridge Univ. Press, 2013).
81. Frederikse, T., Riva, R. E. M. & King, M. A. Ocean bottom deformation due to present-day mass redistribution and its impact on sea level observations. *Geophys. Res. Lett.* **44**, 12306–12314 (2017).
82. Langbein, J. Noise in two-color electronic distance meter measurements revisited. *J. Geophys. Res. Solid Earth* **109**, B04406 (2004).

Author contributions T.F. and F.L. conceived and designed the study. L. Caron and S.A. provided the GIA data and provided guidance on the solid-Earth processes. D.P. provided glacier datasets and helped interpret the underlying uncertainties. V.W.H. provided the TWS reconstruction. P.H. prepared the tide-gauge dataset. L.Z. and L. Cheng helped analyse the steric datasets. Y.-H.W. created the reservoir databases. S.D. provided guidance on the sea-level reconstruction approach. T.F. performed the analysis and wrote the manuscript. All authors contributed to the discussion and helped write the manuscript.
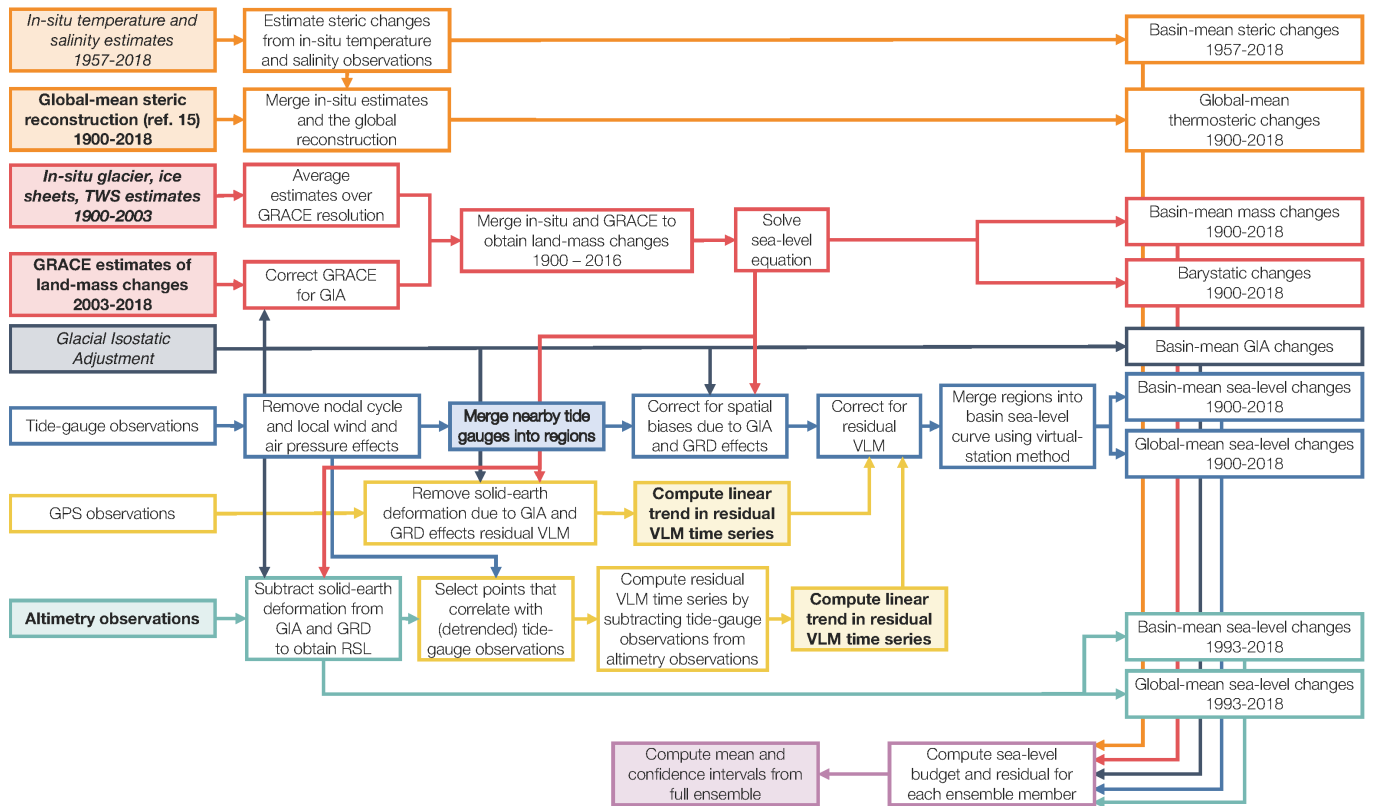
Extended Data Fig. 1 | Schematic overview of the computation of reconstructed sea level and the contributors. Steps with a shaded background involve steps where each ensemble member is perturbed: for steps shown in bold, the estimate is drawn from a probability density function; for steps in italic, the estimate is randomly chosen from a pool of estimates. All the steps are repeated for each of the 5,000 ensemble members, until the final step, where all ensemble members are combined to estimate the mean and confidence interval of the global-mean and basin-mean sea-level budget and its components. Steps and arrows in orange refer to estimates of steric sea level, red refers to estimates of ocean mass, dark blue refers to GIA, light blue refers to tide-gauge observations, yellow refers to VLM, turquoise refers to satellite altimetry, and purple refers to the budget analysis. The global-mean steric reconstruction for 1900–2018 is from ref. [15].
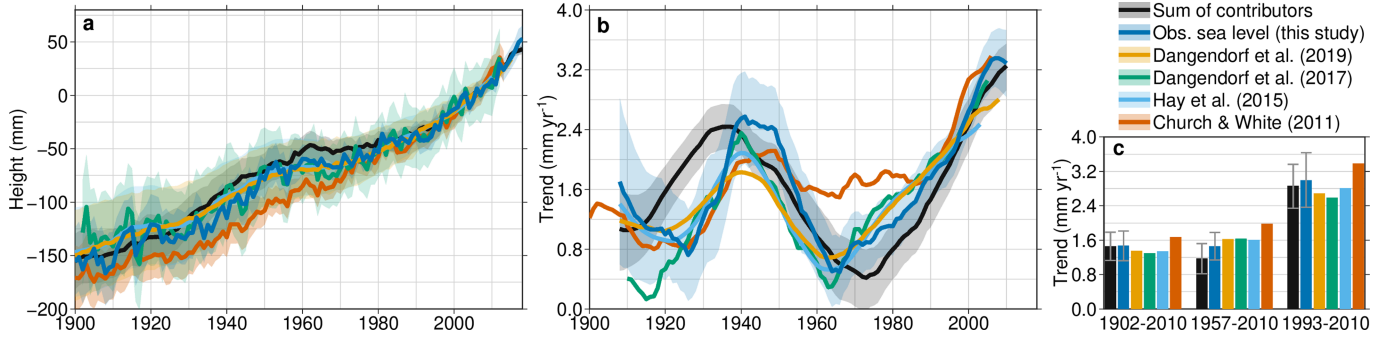
Extended Data Fig. 2 | Comparison with other recent sea-level reconstructions.
All panels show observed GMSL and the sum of contributors from this study
and other recent GMSL reconstructions[4,5,8,20]. **a**, Annual time series and
their 90% confidence intervals. **b**, 30-year-average rates of the GMSL
reconstructions. **c**, Linear trends over the time intervals indicated. The shaded
regions denote the 90% confidence interval. The values are relative to the
2002–2018 mean.
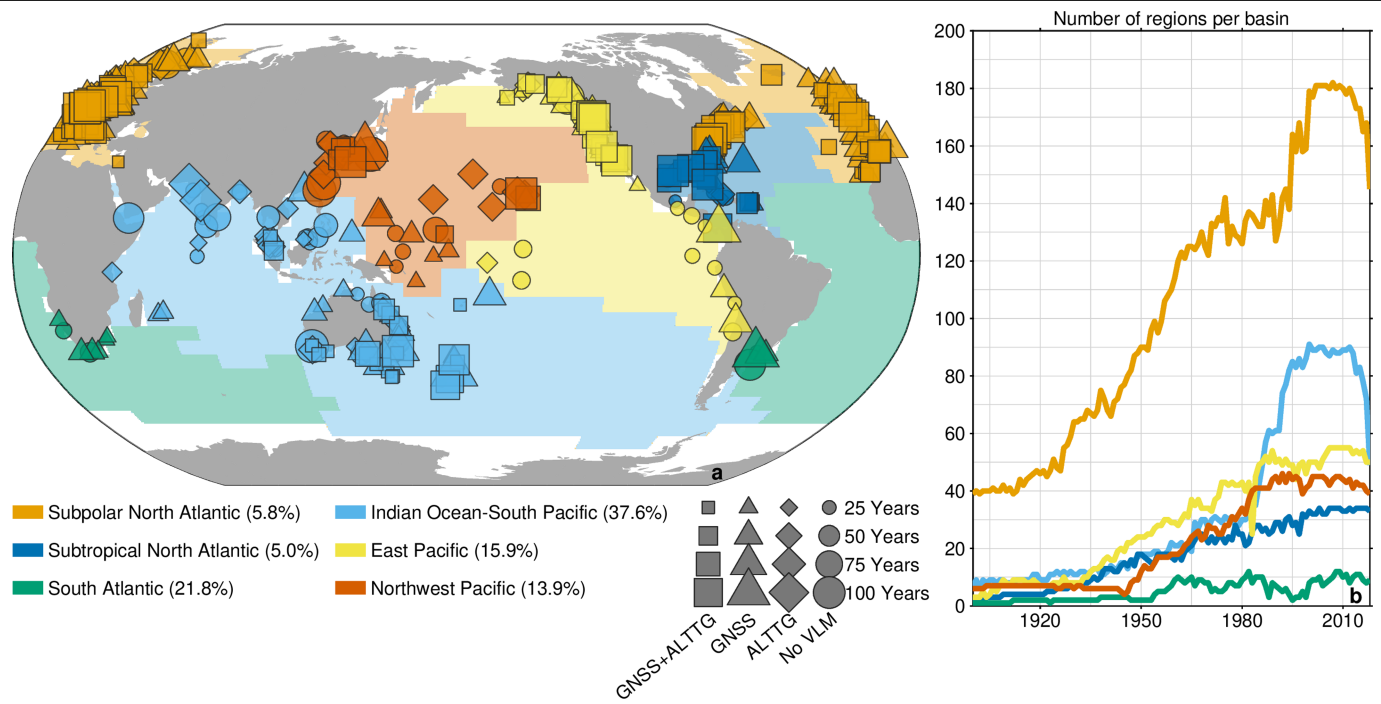
Extended Data Fig. 3 | Map of the regions and basins. a, The ocean basins (shading) and the regions (symbols) that belong to each basin. The shape of the region symbols denotes how the station is corrected for VLM; the size denotes the number of years for which the region provides data. The percentages in the legend show the relative size of the basin as a fraction of the sum of all basins. Each region consists of one tide-gauge station or multiple stations within a 10-km radius. **b**, The number of regions that provide data in a given year for each basin.
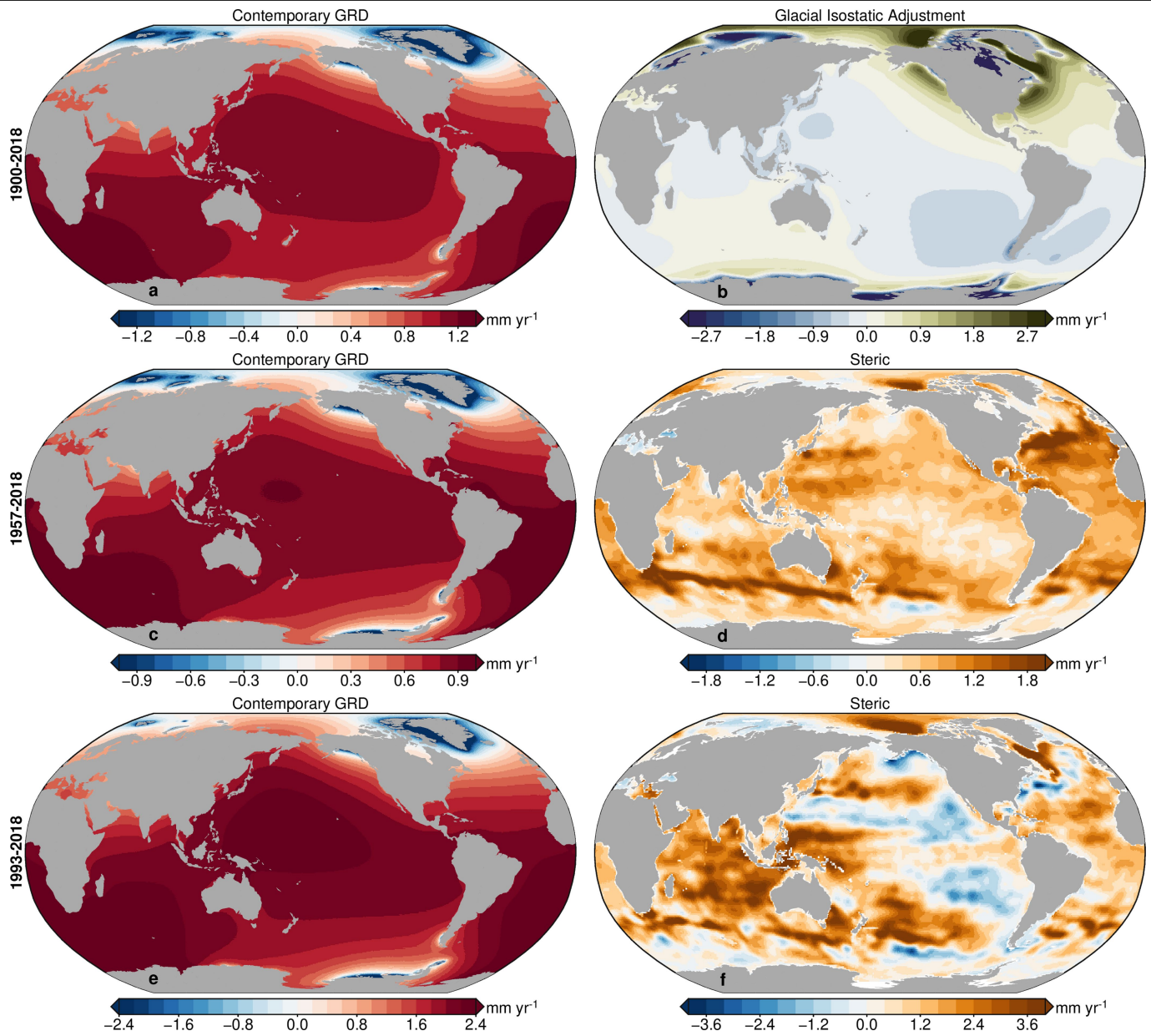
Extended Data Fig. 4 | Linear trends in regional RSL due to ocean-mass changes, GIA and steric changes over three periods. a, **c**, **e**, Local RSL trends due to contemporary GRD effects, for 1900–2018 (**a**), 1957–2018 (**c**) and 1993–2018 (**e**). **b**, RSL changes due to GIA. **d**, **f**, Local steric sea-level changes over 1957–2018 (**d**) and 1993–2018 (**f**). All trends show the ensemble-mean values. The colour scale varies between panels.
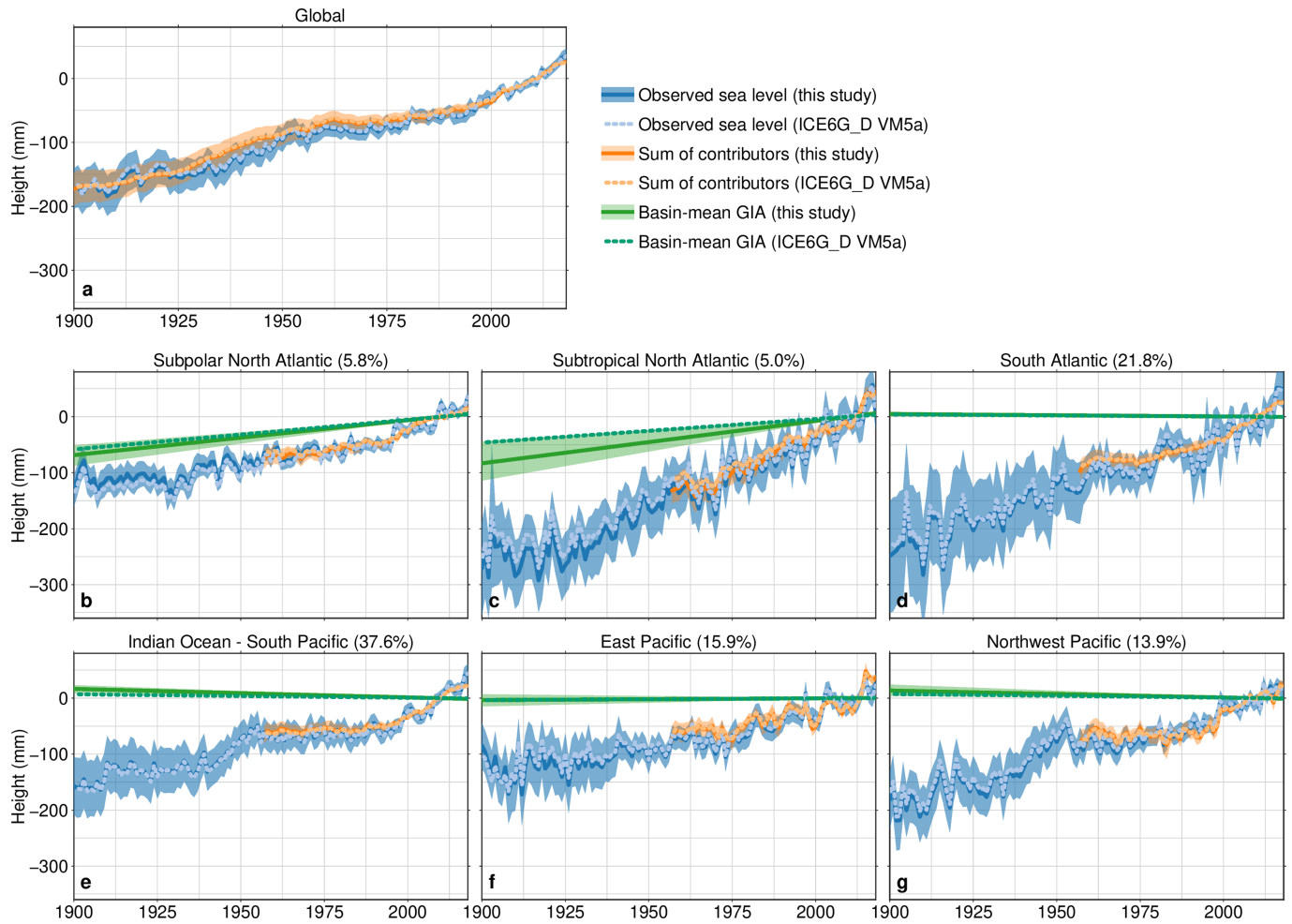
Extended Data Fig. 5 | Comparison of two GIA models. Each panel shows observed sea level, the sum of contributors and the basin-mean sea-level trend due to GIA, using the model used in this study[41] (solid lines) and using the ICE6G D (VM5a) model[42]. Shaded areas indicate 90% confidence intervals. **a**, GMSL. **b**–**g**, Basin-mean sea level.
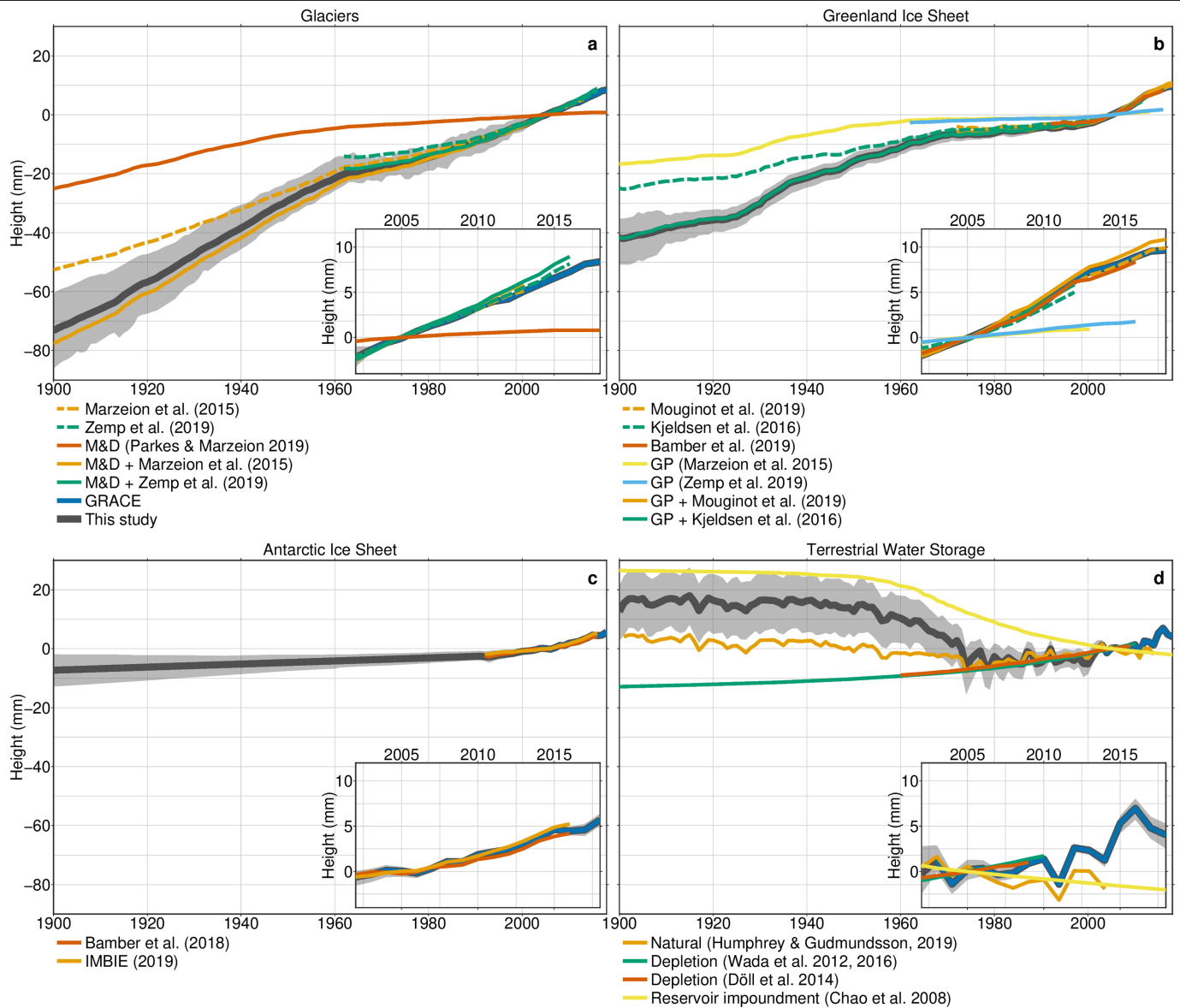
Extended Data Fig. 6 | Central values of individual estimates and our composite final estimate of each barystatic contributor. a, The glacier estimates; data from this study and refs. [16,18,21]. M&D, missing and disappeared glaciers (as determined by ref. [16]). **b**, The Greenland Ice Sheet estimates; data from refs. [14,18,21,24,25]. GP, contribution from Greenland peripheral glaciers.

c, The Antarctic Ice Sheet estimates; data from refs. [23,24]. **d**, The TWS estimates; data from refs. [17,26–28,53]. All estimates are shown relative to the average height over 2003–2005. The inset in each panel shows all the estimates over 2002–2018. Shaded areas indicate 90% confidence intervals.
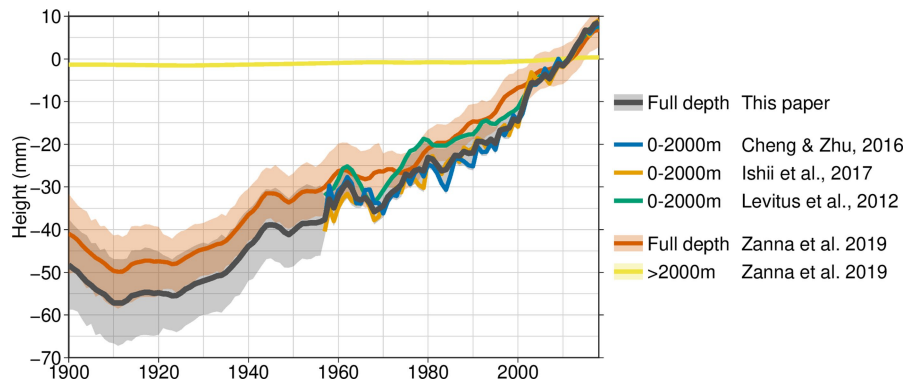
Extended Data Fig. 7 | Individual estimates of global-mean steric sea-level changes. The coloured time series show global-mean steric sea-level changes of each individual estimate[15,30–32] and the averaged estimate used here (black). The shaded areas indicate 90% confidence intervals.

Extended Data Table 1 | Trends in observed basin-mean sea level and its contributors

Subpolar North Atlantic

	1900-2018		1957-2018		1993-2018	
Glaciers	0.42	[0.32 0.52]	0.31	[0.21 0.41]	0.36	[0.28 0.47]
Greenland Ice Sheet	-0.16	[-0.19 -0.13]	-0.11	[-0.14 -0.08]	-0.25	[-0.27 -0.22]
Antarctic Ice Sheet	0.08	[-0.01 0.17]	0.13	[0.04 0.22]	0.33	[0.21 0.45]
Terrestrial Water Storage	-0.14	[-0.23 -0.06]	-0.08	[-0.20 0.03]	0.16	[0.04 0.28]
Barystatic	0.19	[0.05 0.34]	0.25	[0.09 0.41]	0.61	[0.40 0.82]
Glacial Isostatic Adjustment	0.62	[0.47 0.80]	0.62	[0.47 0.80]	0.62	[0.47 0.80]
Steric	-		0.62	[0.40 0.86]	1.18	[1.00 1.37]
Sum of Contributors	-		1.50	[1.10 1.92]	2.42	[2.00 2.82]
Observed sea level	1.08	[0.79 1.38]	1.52	[1.23 1.83]	2.69	[2.18 3.18]
Altimetry	-		-		2.17	[1.66 2.66]

Indian Ocean-South Pacific

	1900-2018		1957-2018		1993-2018	
Glaciers	0.73	[0.55 0.90]	0.56	[0.35 0.72]	0.73	[0.56 0.89]
Greenland Ice Sheet	0.48	[0.39 0.58]	0.33	[0.24 0.42]	0.72	[0.63 0.80]
Antarctic Ice Sheet	0.05	[-0.02 0.12]	0.09	[0.02 0.16]	0.22	[0.13 0.32]
Terrestrial Water Storage	-0.24	[-0.37 -0.11]	-0.17	[-0.34 -0.01]	0.30	[0.11 0.48]
Barystatic	1.03	[0.73 1.34]	0.79	[0.47 1.11]	1.97	[1.61 2.32]
Glacial Isostatic Adjustment	-0.15	[-0.21 -0.08]	-0.15	[-0.21 -0.08]	-0.15	[-0.21 -0.08]
Steric	-		0.64	[0.41 0.87]	1.50	[1.26 1.76]
Sum of Contributors	-		1.29	[0.68 1.91]	3.32	[2.68 3.94]
Observed sea level	1.33	[0.80 1.86]	1.51	[1.03 2.00]	3.93	[3.32 4.55]
Altimetry	-		-		3.65	[3.23 4.08]

Subtropical North Atlantic

	1900-2018		1957-2018		1993-2018	
Glaciers	0.68	[0.50 0.85]	0.50	[0.30 0.65]	0.62	[0.46 0.77]
Greenland Ice Sheet	0.23	[0.18 0.27]	0.15	[0.11 0.20]	0.34	[0.29 0.38]
Antarctic Ice Sheet	0.10	[-0.01 0.20]	0.16	[0.06 0.26]	0.40	[0.26 0.52]
Terrestrial Water Storage	-0.13	[-0.23 -0.03]	-0.05	[-0.18 0.09]	0.28	[0.13 0.43]
Barystatic	0.87	[0.62 1.12]	0.77	[0.50 1.03]	1.63	[1.33 1.92]
Glacial Isostatic Adjustment	0.76	[0.40 1.04]	0.76	[0.40 1.04]	0.76	[0.40 1.04]
Steric	-		1.29	[1.02 1.58]	1.08	[0.60 1.50]
Sum of Contributors	-		2.81	[2.29 3.35]	3.48	[2.72 4.19]
Observed sea level	2.49	[1.89 3.06]	2.76	[2.05 3.42]	3.98	[2.75 5.20]
Altimetry	-		-		4.04	[2.77 5.24]

East Pacific

	1900-2018		1957-2018		1993-2018	
Glaciers	0.66	[0.47 0.85]	0.48	[0.25 0.64]	0.62	[0.44 0.76]
Greenland Ice Sheet	0.48	[0.39 0.58]	0.33	[0.24 0.42]	0.72	[0.63 0.81]
Antarctic Ice Sheet	0.09	[-0.01 0.19]	0.15	[0.05 0.24]	0.37	[0.24 0.49]
Terrestrial Water Storage	-0.22	[-0.34 -0.09]	-0.15	[-0.32 0.02]	0.32	[0.13 0.49]
Barystatic	1.02	[0.70 1.32]	0.81	[0.46 1.13]	2.02	[1.66 2.37]
Glacial Isostatic Adjustment	0.03	[-0.06 0.13]	0.03	[-0.06 0.13]	0.03	[-0.06 0.13]
Steric	-		0.47	[0.21 0.74]	0.37	[-0.01 0.77]
Sum of Contributors	-		1.32	[0.86 1.74]	2.43	[1.90 2.95]
Observed sea level	1.20	[0.76 1.62]	1.64	[1.26 2.03]	1.82	[1.10 2.56]
Altimetry	-		-		2.35	[0.70 4.06]

South Atlantic

	1900-2018		1957-2018		1993-2018	
Glaciers	0.76	[0.56 0.95]	0.56	[0.32 0.73]	0.72	[0.54 0.88]
Greenland Ice Sheet	0.50	[0.41 0.60]	0.34	[0.24 0.43]	0.74	[0.65 0.83]
Antarctic Ice Sheet	0.09	[-0.01 0.19]	0.16	[0.06 0.25]	0.38	[0.26 0.50]
Terrestrial Water Storage	-0.20	[-0.35 -0.05]	-0.12	[-0.30 0.07]	0.38	[0.18 0.58]
Barystatic	1.15	[0.82 1.48]	0.93	[0.58 1.26]	2.23	[1.87 2.61]
Glacial Isostatic Adjustment	-0.04	[-0.08 -0.02]	-0.04	[-0.08 -0.02]	-0.04	[-0.08 -0.02]
Steric	-		0.88	[0.73 1.03]	1.29	[0.98 1.66]
Sum of Contributors	-		1.78	[1.23 2.33]	3.48	[2.79 4.15]
Observed sea level	2.07	[1.36 2.77]	2.17	[1.62 2.73]	3.89	[2.44 5.33]
Altimetry	-		-		3.45	[3.04 3.86]

Northwest Pacific

	1900-2018		1957-2018		1993-2018	
Glaciers	0.69	[0.50 0.88]	0.50	[0.28 0.67]	0.65	[0.47 0.80]
Greenland Ice Sheet	0.53	[0.42 0.64]	0.35	[0.26 0.45]	0.78	[0.68 0.88]
Antarctic Ice Sheet	0.10	[-0.01 0.20]	0.16	[0.06 0.26]	0.40	[0.26 0.53]
Terrestrial Water Storage	-0.22	[-0.36 -0.09]	-0.16	[-0.34 0.02]	0.34	[0.15 0.52]
Barystatic	1.09	[0.76 1.41]	0.86	[0.51 1.21]	2.17	[1.78 2.53]
Glacial Isostatic Adjustment	-0.12	[-0.22 -0.03]	-0.12	[-0.22 -0.03]	-0.12	[-0.22 -0.03]
Steric	-		0.71	[0.45 0.98]	1.20	[0.79 1.58]
Sum of Contributors	-		1.44	[0.80 2.07]	3.23	[2.52 3.93]
Observed sea level	1.68	[1.27 2.09]	1.80	[1.42 2.18]	2.77	[2.11 3.39]
Altimetry	-		-		3.53	[2.64 4.45]

The trends are given in millimetres per year, over 1900–2018, 1957–2018 and 1993–2018. The numbers in brackets indicate the 90% confidence intervals.